



Cite this: *Energy Environ. Sci.*,  
2022, 15, 2983

## Triboelectric-nanogenerator-enabled mechanical modulation for infrared wireless communications†

Zihan Wang, <sup>a</sup> Yuchao Jin, <sup>a</sup> Chengyue Lu, <sup>a</sup> Jiyu Wang, <sup>a</sup> Ziwu Song, <sup>a</sup> Xu Yang, <sup>a</sup> Yidan Cao, <sup>b</sup> Yunlong Zi, <sup>c</sup> Zhong Lin Wang <sup>defg</sup> and Wenbo Ding <sup>ah</sup>

Optical wireless communications (OWC), featuring a wide optical bandwidth and robust resistance to radio-frequency interference (RFI), can benefit the development of the Internet of Things (IoT). Making IoT devices ubiquitous calls for decentralized and on-demand power sources for wireless communications. However, existing visible-light-based self-powered OWC systems are complex on the receiver side, they are easily affected by ambient light, and they can disturb dark environments. In this paper, we realized self-powered infrared (IR) wireless communications via integrating a triboelectric nanogenerator (TENG) and an IR transmitter. With customized mechanical modulation protocols, both the frequency and amplitude features of the IR signal, enabled by different mechanical motion or mechanical structures of TENG devices, can be leveraged for conveying information. The concept of this TENG-enabled wireless infrared communications framework and the results from this study may pave the way for a new generation of self-powered communications in a sustainable manner.

Received 19th March 2022,  
Accepted 7th June 2022

DOI: 10.1039/d2ee00900e

rsc.li/ees

### Broader context

In the era of 6G and the Internet of Things (IoT), massive amounts of data are produced by distributed sensors and transferred wirelessly between various smart devices. Meanwhile, the proportion of global energy expended on communications keeps increasing. A possible solution to reduce energy required for information transfer is harvesting pervasive mechanical energy. However, the popularization of so-far-realized visible-light-based self-powered optical wireless communications (OWC) systems is restricted by ambient light conditions and complex receiver designs. In this work, an infrared (IR)-based OWC system is proposed to leverage a triboelectric nanogenerator (TENG) to achieve information encoding and transmission using an IR signal that is robust against light interference. Specifically, the mechanical motion and mechanical structures of TENGs can be utilized to convey information and power the IR emitter. Moreover, the system supports diverse TENG structures and can accommodate different demands. Our research shows that self-powered IR-based OWC, with the merits of long transmission distances, high adaptability, and low cost, may significantly promote TENG-enabled OWC and pave the way for sustainable communications.

<sup>a</sup> Tsinghua-Berkeley Shenzhen Institute, Tsinghua Shenzhen International Graduate School, Tsinghua University, Shenzhen 518055, China.

E-mail: jiyuwang@sz.tsinghua.edu.cn, ding.wenbo@sz.tsinghua.edu.cn

<sup>b</sup> Institute of Materials Research, Tsinghua Shenzhen International Graduate School, Tsinghua University, Shenzhen 518055, China

<sup>c</sup> Department of Mechanical and Automation Engineering and Shun Hing Institute of Advanced Engineering, The Chinese University of Hong Kong, New Territories, Hong Kong SAR, China

<sup>d</sup> Beijing Institute of Nanoenergy and Nanosystems, Chinese Academy of Sciences, Beijing 101400, China

<sup>e</sup> School of Nanoscience and Technology, University of Chinese Academy of Sciences, Beijing 100049, China

<sup>f</sup> CUSTech Institute of Technology, Wenzhou, Zhejiang 325024, China

<sup>g</sup> School of Materials Science and Engineering, Georgia Institute of Technology, Atlanta, GA 30332-0245, USA. E-mail: zhong.wang@mse.gatech.edu

<sup>h</sup> RISC-V International Open Source Laboratory, Shenzhen 518055, China

† Electronic supplementary information (ESI) available. See DOI: <https://doi.org/10.1039/d2ee00900e>

‡ These authors contributed equally to this work.

### Introduction

Wireless sensing and communications capabilities are essential for any Internet of Things (IoT) infrastructure.<sup>1,2</sup> Since Maxwell predicted the existence of electromagnetic (EM) waves,<sup>3</sup> attempts to push the limits of wireless communications have taken place over a century. However, traditional radio frequency (RF) based communications technologies are limited due to the scarcity of band resources<sup>4</sup> and radio-frequency interference (RFI).<sup>5</sup> Under these circumstances, optical communications methods that leverage the abundant optical bandwidth space have been developed to provide alternative communications approaches.<sup>6</sup> Depending on the transmission medium, optical communications can be divided into fiber-optics communications and optical wireless communications (OWC).<sup>7</sup>

With the merits of a broad frequency spectrum and high capacity, OWC is suitable for high data throughput and massive device access, it is becoming a complementary communication technology for the IoT, and it has been considered as a potential option for 6G telecommunications.<sup>8</sup>

Existing OWC systems, such as visible light communications (VLC) system, aiming to enable always-on high communication rates<sup>9</sup> rely on high-speed control circuits to modulate the illumination from high-brightness light-emitting diodes (LEDs).<sup>10</sup> However, for most IoT applications, with limited energy storage and intermittent communication, traditional OWC systems will consume excessive energy due to their complex circuits and idling state.<sup>11</sup> The emergence of triboelectric nanogenerators (TENGs)<sup>12–15</sup> as mechanical-to-electrical power converters with high instantaneous power outputs has advantages for powering optical transmitters.<sup>16,17</sup> Since the characteristics of mechanical stimuli can determine the output electrical signals of TENGs, encoding a mechanical motion sequence may allow information modulation<sup>18</sup> and significantly reduce the complexity and energy consumption of traditional modulation circuits. Nevertheless, existing visible-light-based self-powered OWC systems still face challenges other than those relating to the power supply. First, the communication rate of the system:<sup>19,20</sup> using a digital camera as a receiver is limited due to the relatively low frame-rate of the camera, while adopting a high-speed camera will lead the overall system away from low-cost and low-energy consumption designs. Second, for systems utilizing photodetectors (PDs) to receive visible light signals, due to ambient light interference, these can only operate within a small distance range.<sup>21–23</sup> Third, visible-light-based approaches may disturb low-light environments in cinemas or bedrooms.

To overcome the performance bottlenecks in visible-light-based self-powered OWC systems (Table S1 (ESI†)), for the first time, we introduce invisible optical carriers (*i.e.*, infrared (IR)) into a self-powered OWC system. The proposed TENG-enabled wireless infrared communications (IR-TENG) framework adopts a low-cost low-energy infrared emitter/receiver to realize an invisible-light self-powered OWC system. Unlike traditional approaches that encode messages into the IR signal using electronic modulation circuits, we propose “mechanical modulation” protocols for the IR-TENG framework, encoding the message into the IR signal *via* mechanical features. Specifically, the mechanical modulation protocols are inspired by classical digital modulation protocols,<sup>24</sup> where messages are encoded into the frequency or amplitude features of the IR signal determined by the mechanical motion or mechanical structure of the TENG devices. Beyond IR-TENG frameworks, the mechanical modulation protocols allow self-powered wireless communications systems to realize on-demand operation, and this approach can reduce circuit-design complexity and avoid standby power consumption between transmissions. To exemplify the applicability of the IR-TENG framework and mechanical modulation protocols, we designed a rotary-freestanding TENG (RF-TENG) device that supports two mechanical modulation protocols. We also demonstrated other TENG devices (*e.g.*, an opposite-charge-enhanced transistor-like triboelectric

nanogenerator (OCT-TENG)<sup>17</sup>) that could be adapted into the IR-TENG framework. With total mechanical-motion-enabled information modulation and transmission abilities, this approach is expected to pave the way for a new generation of self-powered communications and self-powered wireless sensing systems in the era of the IoT.

## Results and discussion

### Concept and workflow of mechanical modulation for self-powered IR communications

The concept of the TENG-enabled infrared communication system is illustrated in Fig. 1a. The system consists of two parts: an all-in-one TENG device capable of directly powering an IR transmitter; and a mechanical modulation protocol for information encoding and decoding. Compared with traditional IR communications,<sup>25</sup> the proposed IR-TENG framework does not rely on an external power supply or complex electrical components. For the mechanical modulation protocol, many kinds of characteristic mechanical stimuli can be utilized to encode information. Inspired by the classic digital modulation protocol, we proposed mechanical frequency modulation (MFM) and mechanical amplitude modulation (MAM) protocols. The MFM protocol follows the principle of frequency shift keying (FSK), where frequency variations in the TENG output that powers the IR transmitter can be used to encode information. The other protocol, MAM, is conceived from binary amplitude shift keying (2ASK). In the MAM protocol, the pulse-like TENG output controls the on-off state of the IR transmitter, which contains the coded information.

Selecting a suitable IR transmitter is also necessary to fully exploit the energy produced by the TENG. Conventional IR communications systems use IR LEDs with a central wavelength of 850 nm or 940 nm as transmitters. Unlike 850 nm IR LEDs, which emit light near the spectrum that is visible to human eyes, 940 nm IR LEDs do not leak faintly visible red light.<sup>26</sup> Additionally, potentially interfering 940 nm light from the sun is mainly absorbed by water vapor in the atmosphere; therefore, this wavelength for communications produces less noise in the daytime.<sup>27</sup> Therefore, we adopted an IR LED with a 940 nm central wavelength integrated with the corresponding receiver in the circuit of the IR-TENG framework, as illustrated in Fig. 1b. Since only forward current emits an IR LED signal, a bridge-rectifier is therefore connected to the RF-TENG output. Furthermore, the output of the IR receiver is read by a standard microcontroller unit (MCU) used for IoT applications. Both the transmitter and receiver have low-cost and low-energy designs and are fully compatible with the existing IoT infrastructure.

### Design and characterization of the RF-TENG

Since the forward current capable of driving the IR LED is on the microampere level,<sup>28</sup> we adopted an RF-TENG that is capable of outputting a high current.<sup>29–34</sup> An exploded view of the RF-TENG is shown in Fig. 2a. The stator and rotator of the RF-TENG are fabricated using printed circuit board (PCB)

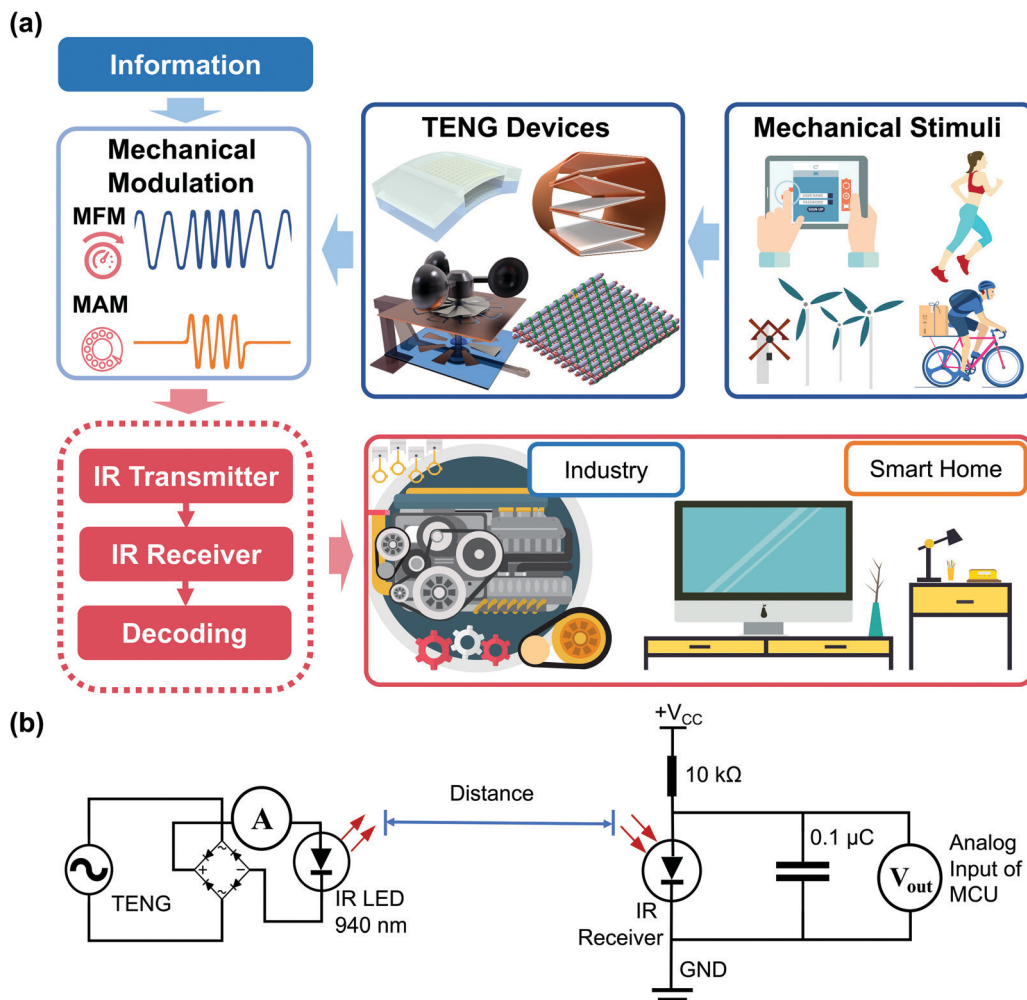


**Fig. 1** (a) A workflow diagram showing the proposed mechanical modulation protocols for the self-powered IR communications system and its applications. Images of the TENG devices are reproduced with permission: copyright 2021, Elsevier;<sup>39</sup> copyright 2021, Association for Computing Machinery;<sup>40</sup> copyright 2018, American Chemical Society;<sup>41</sup> and copyright 2017, John Wiley and Sons.<sup>42</sup> (b) A circuit block diagram of the IR-TENG framework.

technology. The stator features radially arrayed complementary electrodes; the rotator has half the number of electrodes and polytetrafluoroethylene (PTFE) film is attached as the triboelectric layer. Both the rotator and stator PCBs are attached to supporting plates using Velcro, and the plates are attached to the servo motor with bearings and bolts. Photographs of all mechanical components can be found in Fig. S1 (ESI†). The working mechanism of the RF-TENG is depicted in Fig. 2b. In state i, the rotator electrode is entirely in contact with electrode A, which creates positive charge on electrode A due to electrostatic induction. After sliding, the rotator reaches state ii, and the induced positive charge on electrode A decreases while the induced positive charge on electrode B increases. Therefore, the current will flow from electrode A to electrode B until electrostatic balance is established. Therefore, the current will flow from electrode A to electrode B until it reaches state iii, where an electrostatic balance is established. In state iv, the subsequent rotator electrode contacts with electrode A and the previous rotator electrode moves away from

electrode B; current flows from electrode B to electrode A until electrostatic balance is reached again. The continuous rotation of the RF-TENG can be regarded as repeating the above cycle, making it capable of generating an alternating current (AC) output.

To investigate suitable design parameters that can output adequate current to drive the IR LED, we referred to the following equation that governs the short-circuit current output ( $I_{SC}$ ) of the RF-TENG:<sup>30</sup>

$$I_{SC} = 2\pi f N \sigma_0 (r_{out}^2 - r_{in}^2), \quad (1)$$

where  $f$  is the rotation rate of the RF-TENG,  $N$  is the number of gratings,  $\sigma_0$  is the charge density of the triboelectric material, and  $r_{out}$  and  $r_{in}$  are the outer and inner radii of the TENG electrode gratings, respectively. Based on previous work,<sup>35</sup> although increasing the number of gratings can theoretically boost the current output, the equivalent internal capacitance of the TENG formed from adjacent stator electrodes will also increase, thereby inhibiting the output current. To investigate

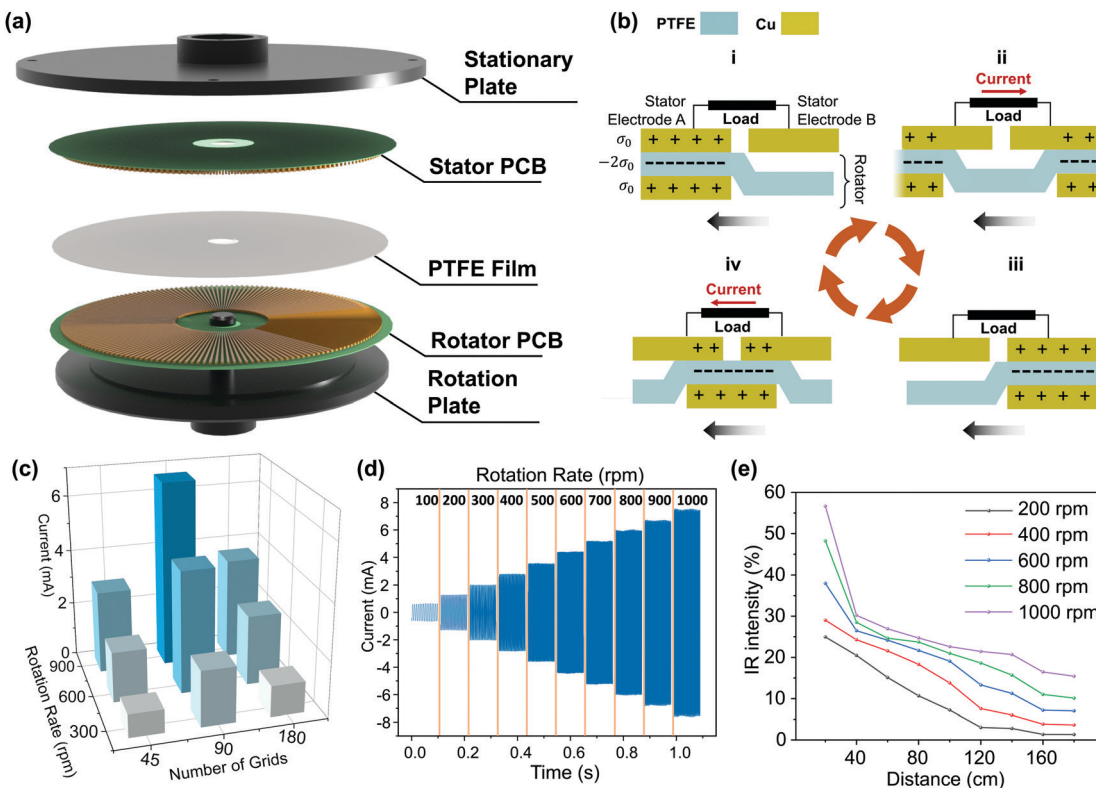


**Fig. 2** (a) An exploded view diagram of the RF-TENG. (b) Schematic diagrams illustrating the four stages of the RF-TENG. Note that PTFE film is affixed to the rotator PCB. (c) The peak values of short-circuit currents generated using different PCB designs and rotation rates. (d) Short-circuit currents at rotation rates from 100 rpm to 1000 rpm. (e) The peak values of IR intensity read by the receiver at different rotation rates and distances.

the number of gratings that can maximize the current output, we considered three PCB designs with 45, 90, or 180 gratings on the rotator PCB and twice the number on the stator PCB (Fig. S2, ESI†). As illustrated in Fig. 2c, the 90-grating rotator outperforms the other two rotators at three different rotation rates. Further optimization of the shape of the electrodes resulted in the design of a rotary freestanding-electret generator,<sup>36</sup> where equal-interval electrodes reduce intrinsic capacitance of the inner radius and maximize the effective area of the outer radius. The subsequent experiments and applications of the RF-TENG utilize the 90-grating design.

From the perspective of the power supply, the current output of the RF-TENG was characterized at rotation rates from 100 to 1000 rotations per minute (rpm). As shown in Fig. 2d, the short-circuit current output increases at a higher rotation rate. To investigate the capability of using the RF-TENG to drive the IR transmitter, we measured the peak value of the IR intensity upon varying the transmitter-to-receiver distance from 20 cm to 180 cm at five different rotation rates. The IR intensity is defined using eqn (2):

$$\text{IR}_{\text{intensity}} = \frac{V_{\text{CC}} - V_{\text{out}}}{V_{\text{CC}}} \times 100\%. \quad (2)$$

The results are plotted in Fig. 2e; the IR intensity at the receiver decreases at longer distances and slower rotation rates.

The results show that the RF-TENG can drive an IR transmitter for communications over a relatively long distance.

#### Application of mechanical frequency modulation

The workflow for mechanical frequency modulation is illustrated in Fig. 3a. On the transmitter side, the message to be sent is first encoded into a sequence of ASCII values. Then, the sequence is linearly mapped to a series of servo motor rotation rates. The servo motor drives the RF-TENG according to the rotation rate sequence to power the IR LED. On the receiver side, the frequency of the received IR signal is first analyzed via fast Fourier transform (FFT). Then, the sequence of frequency variations is linearly mapped into the ASCII value sequence. Finally, the ASCII sequence is decoded to recover the message. The relationship between the IR signal frequency  $f_{\text{IR}}$  and the rotation rate  $N$  of the adopted 90-grating RF-TENG follows eqn (3):

$$N = \frac{f_{\text{IR}} \times 60\text{s}}{90 \text{ cycles} \times 2} = \frac{f_{\text{IR}}}{3}, \quad (3)$$

which is also confirmed based on the measured results shown in Fig. 3b.

Since each ASCII character comprises two hexadecimal digits, we let the IR transmitter send one hexadecimal digit at a time. To ensure the output of the adopted RF-TENG is sufficient to power the particular IR LED for stable long-distance transmission, we defined the linear mapping (eqn (4)) of each hexadecimal

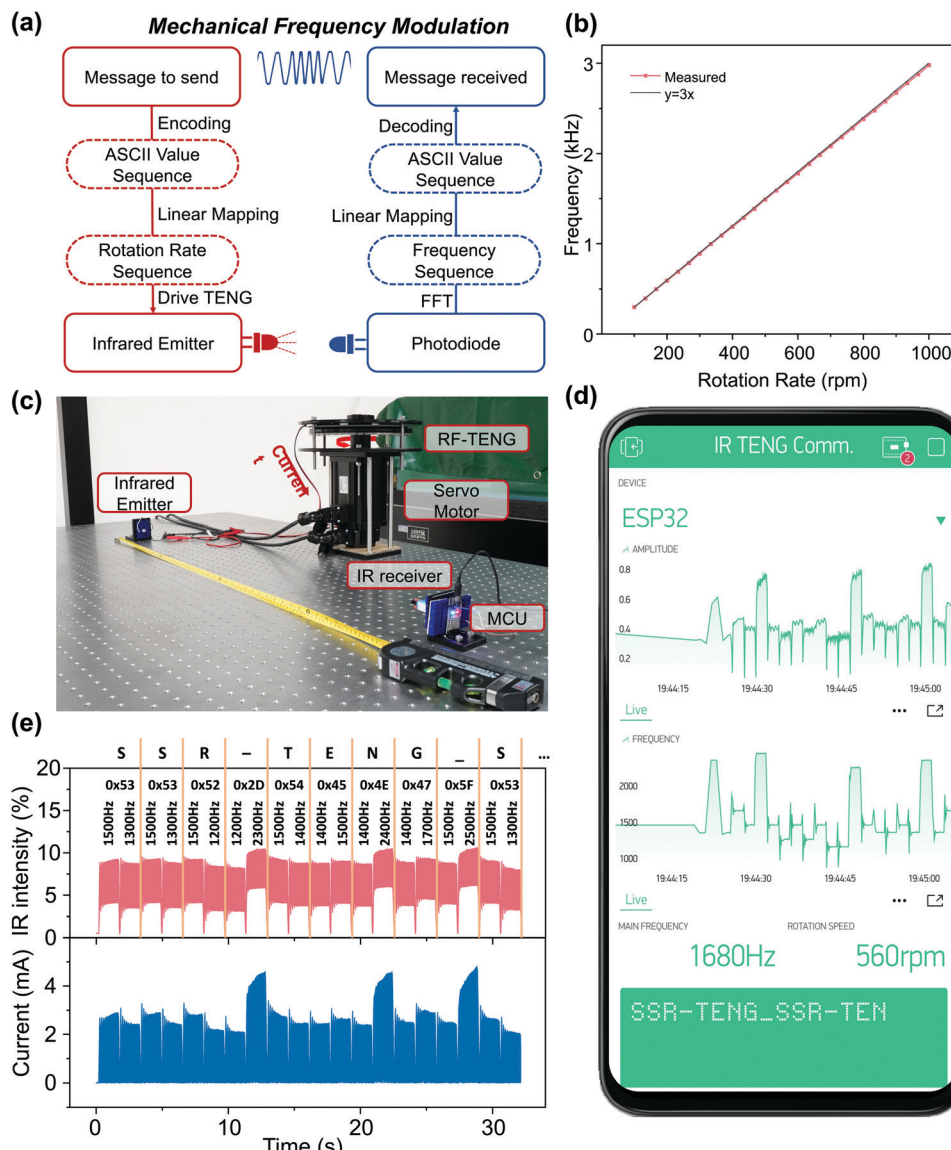


**Fig. 3** (a) A workflow diagram of mechanical frequency modulation. (b) The relationship between the frequency of the received IR signal and the rotation rate of the servo motor. (c) Experiment setup for mechanical frequency modulation communications using the RF-TENG. (d) A smartphone interface for self-powered IR communications via mechanical frequency modulation. (e) The measured currents and received IR signals obtained via commencing the rotation rate sequence representing the characters "SSR-TENG\_".

digit (Hex) to a corresponding IR signal frequency, starting from 1 kHz:

$$f_{\text{IR}} = 1000 + 100 + \text{Hex}. \quad (4)$$

To demonstrate the feasibility of mechanical frequency modulation, we used the experimental setup in Fig. 3c and programmed the rotation of the servo motor to transmit the characters "SSR-TENG\_". The received IR signal and simultaneously measured current values are shown in Fig. 3e. Here, the two-digit hexadecimal number that corresponds to the ASCII value of each character and the frequency mapping are labeled. The frequency sequence and character string are transmitted in real-time to a smartphone graphical user interface (GUI) via the

MCU, as shown in Fig. 3d. The video in Movie S1 (ESI†) demonstrates that mechanical frequency modulation can achieve stable character transmission with a distance of 150 cm between the IR LED and the receiver. Moreover, the average signal-to-noise ratio (SNR) when transmitting the message via mechanical frequency modulation at a distance of 150 cm is 27.28 dB. As far as the authors know, this is the longest communication distance realized with a self-powered OWC system. The algorithm for SNR calculations can be found in Note S1 (ESI†).

Apart from sending messages, the linear frequency response of the TENG-driven IR transmitter (Fig. 3b) can also be leveraged for wireless rotation-rate monitoring. Such measurements do not rely on an external power supply and the optical wireless

transmission does not create or is not affected by RFI, which is especially useful in facilities like radio telescope arrays or radar stations.

### Applications of mechanical amplitude modulation

The proposed mechanical amplitude modulation is achieved *via* modifying the amplitude or simply using the on-off states of the TENG output to encode information. Fig. 4a depicts the workflow of mechanical amplitude modulation. Since amplitude modulation is less resilient to environmental noise,<sup>37</sup> we incorporated channel coding, a technique used in digital communications to improve system robustness, into the mechanical amplitude modulation protocol. The idea of channel coding is to add redundant information to the original message to allow the receiver to detect and correct errors. In our proof-of-concept application, extended Hamming code,<sup>38</sup> a classical

algorithm that has been widely deployed in modern communications systems, is adopted for error checking and correction (ECC). Moreover, by alternating the rotation rate of the RF-TENG, the system is capable of transmitting messages to different receivers.

As Fig. 4b illustrates, the RF-TENG is modified for mechanical amplitude modulation *via* adding a structure modulation plate (Fig. S3, ESI†) and a microswitch (Fig. S4, ESI†). The microswitch lever that contacts the perimeter of the modulation plate controls the circuit, starting or stopping IR transmission. Thus, the on-off state of signal transmission can be controlled *via* configuring flat or concave blocks on the mechanical amplitude modulation plate. For demonstration, we programmed the mechanical amplitude modulation plate with three configurations (Fig. S5, ESI†), representing television channels or other machine operation codes that users would

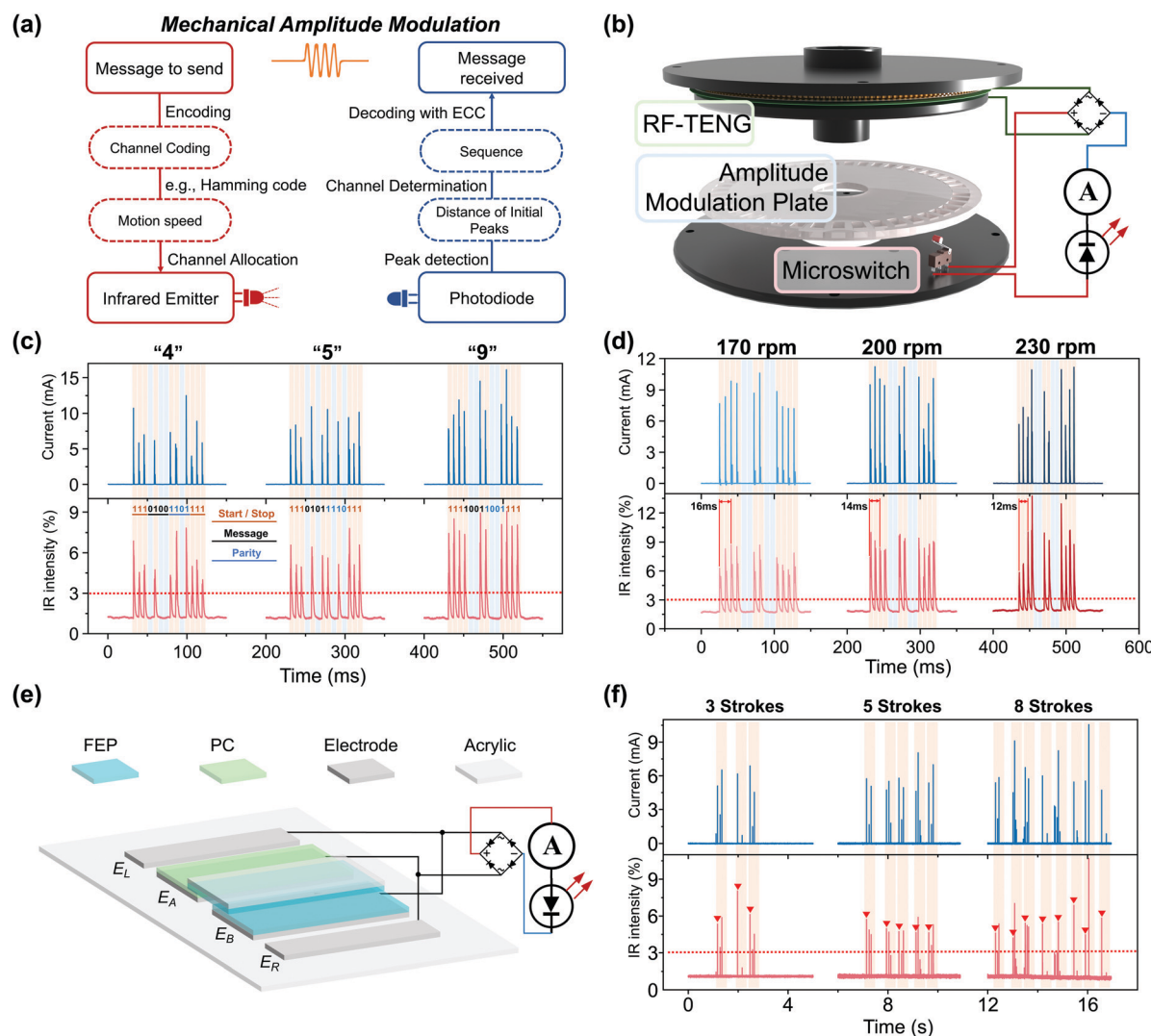


**Fig. 4** (a) A workflow diagram of mechanical amplitude modulation. (b) A modified RF-TENG for mechanical amplitude modulation communication. (c) The measured currents and received IR signals corresponding to the numbers “4”, “5”, and “9” with channel coding. (d) The measured currents and received IR signals of the number “9” with channel coding at different rotation rates. (e) The structure of the OCT-TENG. (f) The measured currents and received IR signals correspond to different sliding strokes with the OCT-TENG.

like to command. Here, the bit sequence is composed of three parts: the first and last three bits are treated as start or end transmission symbols; the initial four bits after the start transmission symbol is the message to be sent; and the following four bits are parity bits generated by the extended Hamming code. A detailed description of the extended Hamming code can be found in Note S2 (ESI<sup>†</sup>). The corresponding current outputs and IR intensity readings are illustrated in Fig. 4c. The process of reconfiguring the mechanical amplitude modulation plate and sending the pulse sequence to control the LED segment display is shown in Movie S2 (ESI<sup>†</sup>). Upon changing the rotation rate of the RF-TENG, the frequency of the transmission signal varies. As illustrated in Fig. 4d, the same starting symbol showed different time durations at different rotation rates. The frequency feature calculated from the starting symbol is utilized to identify communication channels. Once the calculated frequency matches the identification frequency of a particular channel, that channel will proceed with information decoding. Movie S3 (ESI<sup>†</sup>) demonstrates that three receivers, as illustrated in Fig. S6 (ESI<sup>†</sup>), can successfully decode messages only in response to their corresponding identification frequency. According to the algorithm described in Note S1 (ESI<sup>†</sup>), the SNR of transmission *via* mechanical amplitude modulation with the RF-TENG at a 60 cm distance is 25.57 dB. Since 45 holes are punctured into the perimeter of the modulation plate and considering the start/end symbol and parity bits, a maximum of  $2^{19}$  instructions can be encoded on a single plate; such a large instruction set can even be used to encode complex commands.

In addition to the RF-TENG, other TENG devices with adequate output currents that can drive IR-LEDs can also be incorporated into the IR-TENG framework. Here, we adopt an opposite-charge-enhanced transistor-like triboelectric nanogenerator (OCT-TENG),<sup>17</sup> a small device with high instantaneous current output, to exemplify the idea in the context of mechanical amplitude modulation. The structure of the OCT-TENG-powered IR transmitter is illustrated in Fig. 4e. Each sliding stroke can generate several IR pulses (Fig. 4f). At a distance of 40 cm, the number of sliding strokes can be interpreted *via* setting a threshold and suitable detection time intervals (Movie S4, ESI<sup>†</sup>). This shows that TENGs with miniaturized structures can also leverage an IR transmitter to send simple instructions, and this is adequate for most IoT-enabled smart home applications such as adjusting a thermostat, switching a light on or off, and opening curtains. Since IR receivers are already widely applied in industry and home environments to control industrial machines, home appliances, and other IoT gadgets, this IR-TENG framework is expected to provide a sustainable alternative solution to remote controls with batteries. Due to its flexible design and the nature of its self-powered communication, this will further promote the goal of carbon neutralization.

## Conclusions

This work proposed a triboelectric-nanogenerator-enabled self-powered infrared communications (IR-TENG) framework and

mechanical modulation protocols for information modulation. The TENG device in the framework works both as the power source and information source, and it is combined with an IR LED to form a complete wireless transmission unit without introducing complicated power management and signal modulation circuits. Inspired by classical digital modulation used in electromagnetic wave communications (*i.e.*, FSK and 2ASK), the information encoded *via* the mechanical modulation approach can involve continuous or intermittent mechanical motion. *Via* considering the relationship between the rotation rate and the frequency of the IR signal, the mechanical frequency modulation approach demonstrates its capability for wireless transmission over 150 cm. For mechanical amplitude modulation, the adoption of channel coding improved the robustness of using a pulse-like TENG signal for communications. We also demonstrate that the IR-TENG set-up can utilize TENG devices other than the RF-TENG (*e.g.*, OCT-TENG). In practical terms, the design parameters of the device adopted in the IR-TENG framework can be optimized to accommodate specific applications. The concept and results of this work may broaden the application of self-powered wireless sensing and communications *via* integrating invisible-light transmission and mechanical modulation protocols.

## Experimental

### Fabrication of the RF-TENG

The rotor of the RF-TENG is made *via* adhering 80 µm-thick PTFE film to a rotor PCB. Both the rotor and stator PCBs are made of a 1.6 mm-thick FR-4 substrate with 35 µm-thick copper foil. The radii of the rotator and stator PCB boards are 125 mm and 135 mm, respectively, and an extra radius on the perimeter of the stator board is reserved for the solder pad connected to the output wires to prevent collation with the rotator. The radii of the copper electrodes for both PCBs range from  $r = 35$  mm to  $r = 120$  mm. The stationary plate ( $r = 150$  mm), rotation plate ( $r = 125$  mm), and support plate ( $r = 150$  mm) were machined from anodized aluminum. The mechanical amplitude modulation plate ( $r = 125$  mm), made of 5 mm-thick acrylic (polymethylmethacrylate, PMMA) attached to the bottom side of the rotation plate, was laser cut (Hans Laser CMA0604-B-A) with fan-shape holes of 5° and separated at 3° on its perimeter. The flat blocks were collected from the fan-shape laser cutting residuals, while the concave blocks were made *via* 3D printing. The microswitch is fixed to an acrylic holder and bolted to the support plate.

### Fabrication of the OCT-TENG

The slider of the OCT-TENG is made *via* affixing 100 µm-thick FEP (fluorinated ethylene propylene) film (50 mm × 50 mm) to an acrylic substrate of the same size. A sponge was used between the FEP film and substrate to maintain soft contact. Electrode  $E_A$  and electrode  $E_B$  on the stator are made of 100 µm-thick PC (polycarbonate) (50 mm × 50 mm) and FEP film, respectively. The conductive wire and stator film are taped to

the acrylic flat substrate using double-sided adhesive conductive fabric. The conductive electrodes  $E_L$  and  $E_R$  are made of single-sided adhesive conductive fabric connected with conductive wires. A photograph of the OCT-TENG can be found in Fig. S7 (ESI<sup>†</sup>).

### Electrical measurements

The short-circuit current was measured using a Keithley 6514 system electrometer. The readings from the electrometer were recorded using a National Instrument Compact DAQ module (NI 9223). V-I curve and forward current supply measurements from the 940 nm IR LED (Fig. S8 (ESI<sup>†</sup>)) are performed using a Keithley 6514 system electrometer and SIGLENT SPD3303C programmable source meter.

### Signal processing and software interface

The IR reading circuit was connected to an ESP-32 MCU as a power supply and for analog-to-digital conversion. Then, the MCU implemented signal processing, including denoising, frequency analysis, segmentation, and decoding, via the Espressif DSP Library. Finally, the MCU sent the result via the built-in BLE module to a smartphone. Pseudocode for the algorithm running on the MCU can be found in Note S3 (ESI<sup>†</sup>). The graphical user interface (GUI) on the smartphone for mechanical frequency modulation was built on Blynk, an open-source IoT platform.

### Author contributions

Z. W. and W. D. conceived the idea; J. W., Z. L. W., and W. D. conducted the work and supervised the experiments; Z. W. and Y. J. prepared the manuscript; Y. J., Z. S., and X. Y. designed and fabricated the device; Z. W. and C. L. helped with electrical measurements and application demonstration; Y. Z. and Y. C. helped modify the manuscript. All the authors discussed the results and commented on the manuscript.

### Conflicts of interest

The authors declare that they have no known competing financial interests or personal relationships that could have influenced the work reported in this paper.

### Acknowledgements

Z. W., Y. J., and C. L. contributed equally to this work. This work is supported in part by the National Natural Science Foundation of China under Grants 62104125 and 52007019, by the Guangdong Basic and Applied Basic Research Foundation 2020A1515110887, by the grant from the Institute for Guo Qiang of Tsinghua University 2020GQG1004, and by Tsinghua Shenzhen International Graduate School (HW2021005, QD2021013C and JC2021007).

## References

- 1 A. Burg, A. Chatopadhyay and K. Y. Lam, *Proc. IEEE*, 2018, **106**, 38–60.
- 2 J. Li, C. Wu, I. Dharmasena, X. Ni, Z. Wang, H. Shen, S. L. Huang and W. Ding, *Intell. Conv. Netw.*, 2020, **1**, 115–141.
- 3 J. C. Maxwell, *Proc. R. Soc. London*, 1864, 531–536.
- 4 G. Zhou, J. A. Stankovic and S. H. Son, *IEEE EmNets*, 2006, **6**.
- 5 E. G. Njoku, P. Ashcroft, T. K. Chan and L. Li, *IEEE Trans. Geosci. Remote Sens.*, 2005, **43**, 938–947.
- 6 R. Essiambre and R. W. Tkach, *Proc. IEEE*, 2012, **100**, 1035–1055.
- 7 S. Hranilovic, *Wireless Optical Communication Systems*, Springer Science & Business Media, 2006.
- 8 M. Z. Chowdhury, M. K. Hasan, M. Shahjalal, M. T. Hossan and Y. M. Jang, *IEEE Commun. Surv. Tutor.*, 2020, **22**, 930–966.
- 9 J. Song, W. Ding, F. Yang, H. Yang, B. Yu and H. Zhang, *IEEE Trans. Broadcast.*, 2015, **61**, 299–308.
- 10 S. Rajbhandari, J. J. McKendry, J. Herrnsdorf, H. Chun, G. Faulkner, H. Haas, I. M. Watson, D. O'Brien and M. D. Dawson, *Semicond. Sci. Technol.*, 2017, **32**, 023001.
- 11 J. Rodríguez, D. G. Lamar, P. F. Miaja, D. G. Aller and J. Sebastián, *IEEE Trans. Power Electron.*, 2019, **34**, 1726–1743.
- 12 Z. L. Wang, *Faraday Discuss.*, 2014, **176**, 447–458.
- 13 C. Wu, A. C. Wang, W. Ding, H. Guo and Z. L. Wang, *Adv. Energy Mater.*, 2019, **9**, 1802906.
- 14 C. Chen, Z. Wen, J. Shi, X. Jian, P. Li, J. T. W. Yeow and X. Sun, *Nat. Commun.*, 2020, **11**, 4143.
- 15 H. Lei, Y. Chen, Z. Gao, Z. Wen and X. Sun, *J. Mater. Chem. A*, 2021, **9**, 20100–20130.
- 16 W. Xu, H. Zheng, Y. Liu, X. Zhou, C. Zhang, Y. Song, X. Deng, M. Leung, Z. Yang, R. X. Xu, Z. L. Wang, X. C. Zeng and Z. Wang, *Nature*, 2020, **578**, 392–396.
- 17 H. Wu, S. Wang, Z. Wang and Y. Zi, *Nat. Commun.*, 2021, **12**, 5470.
- 18 H. Guo, J. Zhao, Q. Dong, L. Wang, X. Ren, S. Liu, C. Zhang and G. Dong, *Nano Energy*, 2019, **56**, 391–399.
- 19 W. Ding, C. Wu, Y. Zi, H. Zou, J. Wang, J. Cheng, A. C. Wang and Z. L. Wang, *Nano Energy*, 2018, **47**, 566–572.
- 20 A. Chandrasekhar, V. Vivekananthan, G. Khandelwal and S. J. Kim, *Nano Energy*, 2019, **60**, 850–856.
- 21 J. Huang, X. Yang, J. Yu, J. Han, C. Jia, M. Ding, J. Sun, X. Cao, Q. Sun and Z. L. Wang, *Nano Energy*, 2020, **69**, 104419.
- 22 Z. Tian, L. Su, H. Wang, H. Wang and Y. Zi, *Adv. Opt. Mater.*, 2021, 2102091.
- 23 A. Yu, X. Chen, R. Wang, J. Liu, J. Luo, L. Chen, Y. Zhang, W. Wu, C. Liu, H. Yuan, M. Peng, W. Hu, J. Zhai and Z. L. Wang, *ACS Nano*, 2016, **10**, 3944–3950.
- 24 F. Xiong, *Digital Modulation Techniques*, Artech House, Inc., 2006.
- 25 J. M. Kahn and J. R. Barry, *Proc. IEEE*, 1997, **85**, 265–298.
- 26 H. Kitabayashi, Y. Kawabata, H. Matsubara, K.-I. Miyahara and S. Tanaka, *SEI Tech. Rev.*, 2010, **70**, 71.
- 27 H. Manor and S. Arnon, *Appl. Opt.*, 2003, **42**, 4285–4294.
- 28 E. F. Schubert, *Light-Emitting Diodes*, Cambridge University Press, Cambridge, 2nd edn, 2006.

- 29 P. Chen, J. An, R. Cheng, S. Shu, A. Berbille, T. Jiang and Z. L. Wang, *Energy Environ. Sci.*, 2021, **14**, 4523–4532.
- 30 C. Han, C. Zhang, W. Tang, X. Li and Z. L. Wang, *Nano Res.*, 2014, **8**, 722–730.
- 31 L. Lin, S. Wang, Y. Xie, Q. Jing, S. Niu, Y. Hu and Z. L. Wang, *Nano Lett.*, 2013, **13**, 2916–2923.
- 32 Y. Bai, L. Xu, S. Lin, J. Luo, H. Qin, K. Han and Z. L. Wang, *Adv. Energy Mater.*, 2020, **10**, 2000605.
- 33 J. Cheng, W. Ding, Y. Zi, Y. Lu, L. Ji, F. Liu, C. Wu and Z. L. Wang, *Nat. Commun.*, 2018, **9**, 3733.
- 34 A. Ghaderiaram, A. Bazrafshan, K. Firouzi and M. Kolahdouz, *Nano Energy*, 2021, **87**, 106170.
- 35 M. Bi, Z. Wu, S. Wang, Z. Cao, Y. Cheng, X. Ma and X. Ye, *Nano Energy*, 2020, **75**, 104968.
- 36 Z. Wu, S. Wang, Z. Cao, R. Ding and X. Ye, *Nano Energy*, 2021, **83**, 105787.
- 37 J. Oetting, *IEEE Trans. Commun.*, 1979, **27**, 1752–1762.
- 38 R. W. Hamming, *Bell Syst. Tech. J.*, 1950, **29**, 147–160.
- 39 Y. Luo, Z. Wang, J. Wang, X. Xiao, Q. Li, W. Ding and H. Y. Fu, *Nano Energy*, 2021, **89**, 106330.
- 40 J. Li, Z. Wang, Z. Zhao, Y. Jin, J. Yin, S.-L. Huang and J. Wang, presented in part at the ACM UbiComp, Virtual, Global, September, 2021.
- 41 J. Wang, W. Ding, L. Pan, C. Wu, H. Yu, L. Yang, R. Liao and Z. L. Wang, *ACS Nano*, 2018, **12**, 3954–3963.
- 42 K. Dong, J. Deng, Y. Zi, Y.-C. Wang, C. Xu, H. Zou, W. Ding, Y. Dai, B. Gu, B. Sun and Z. L. Wang, *Adv. Mater.*, 2017, **29**, 1702648.